ECS Transactions, 53 (1) 17-26 (2013)
10.1149/05301.0017ecst ©The Electrochemical Society

Growth Kinetics and Uniform Scaling-up of Graphene Synthesis

K. Celebi[1], M. T. Cole[2,3], N. Rupesinghe[3], P. Greenwood[3], L. Tao[4], D. Akinwande[4], J. Robertson[2], H. G. Park[1*], and K. B. K. Teo[3**]

[1] Department of Mechanical and Process Engineering, ETH Zurich, Zurich CH-8092, Switzerland
[2] Department of Engineering, Electrical Engineering Division, University of Cambridge, Cambridge CB30FA, UK
[3] Aixtron Ltd. Nanoinstruments, Swavesey, Cambridge CB244FQ, UK
[4] Department of Electrical and Computer Engineering, University of Texas at Austin, Austin, Texas 78712, USA

* parkh@ethz.ch
** k.teo@aixtron.com

Chemical vapor deposition on copper is the most widely used method to synthesize graphene at large scale. However, the clear understanding of the fundamental mechanisms that govern this synthesis is lacking. Using a vertical-flow, cold-wall reactor with short gas residence time we observe the early growths to study the kinetics of chemical vapor deposition of graphene on copper foils and demonstrate uniform synthesis at wafer scale. Our results indicate that the growth is limited by the catalytic dissociative dehydrogenation on the surface and copper sublimation hinders the graphene growth. We report an activation energy of 3.1 eV for ethylene-based graphene synthesis.

Introduction

Graphene synthesis on copper by chemical vapor deposition (CVD) has recently become a common choice for obtaining high quality transferable graphene at large scale (1, 2). However, utilization of such large area graphene in many applications requires optimization of the CVD processes in order to obtain good quality domains that offer high degrees of lattice interconnectivity, (3-5) and uniform morphology. Many empirical studies have shown the derivation of high-quality, low-defect density CVD derived graphene, (6) however a deeper understanding of the mechanisms of graphene growth on inexpensive, widely available copper substrates is crucial to achieve generalizations in the systematic optimization of the CVD processes involved to ensure its adoption in a commercial context.

The studies on graphene CVD mechanism on copper so far have shown that surface catalysis would be the dominant growth avenue on copper (7). A low energy electron diffraction study has demonstrated strong interaction of the substrate and graphene flakes during the growth, causing flake shape to become a four-lobed polycrystalline structure under low pressure CVD (LPCVD) (8) whereas hexagonally shaped flakes have been

Downloaded on 2016-02-09 to IP 131.111.5.15 address. Redistribution subject to ECS terms of use (see ecsdl.org/site/terms_use) unless CC License in place (see abstract).

obtained by atmospheric pressure CVD (APCVD) (9). However, not many studies have mentioned about a general kinetics model for the graphene growth. A more recent experimental study based on a methane precursor has claimed carbon adatom attachment to be the rate-limiting step for the graphene growth on copper and explained the kinetics by an Avrami monomolecular model of crystallization (10, 11). In the more advanced field of single-walled carbon nanotube growth, though, there exists compelling evidence of asymmetric sigmoidal growth kinetics (12) that invokes a Gompertz model (13). Indeed, the Gompertz model has long been used to explain other types of crystallization kinetics, such as fat and oil crystallization (14-17).

Here, we observe the graphene flake evolution by resolving the early evolution of the flake morphology and check the valid form of the kinetic curve for our ethylene-based growths. We systematically vary the time and temperature of the CVD process in order to obtain the individual flake data. The data is analyzed to obtain the general functions that govern the kinetics and the activation energy of the growth. We also demonstrate the uniform growth of monolayer graphene over 6-inch wafers.

Experimental

Copper foils were first reduced at 900°C (measured by infrared ratio pyrometer) using a 20-sccm flow of H_2, diluted by 1500-sccm of Ar for a duration of 30 minutes. This step was the same for all growths in order to start the growth on similar copper grain size and crystallographic orientation, which affects the graphene quality (18). After about 2 min of temperature re-stabilization, the reduction was followed by 0.5-4 min growth at varied temperatures with an addition of 7 sccm of ethylene (C_2H_4) without altering the H_2 and Ar flows. The C_2H_4 flow was stopped immediately before the cooling step, to prevent precursor pyrolysis at lower temperatures. (Figure 1a) H_2 was kept flowing until the temperature reached down to 400°C, in order to prevent oxidation that can happen due possibly to the trace amount of moisture inside the chamber. According to our control experiments, this low H_2 partial pressure during the cooling does not cause an observable difference in the average graphene flake size. The total pressure of the chamber was 3.6 mbar, causing less copper sublimation compared to an LPCVD process, thus reducing the detrimental effect of the copper sublimation on graphene.

All growths were carried out by use of a commercial, vertical-flow, cold-wall CVD system (*Black Magic Pro System* by AIXTRON). As we heat the samples from below in the vertical chamber, the gases incoming from above enter an ascending temperature gradient. However, this gradient neither causes hydrogenation nor decomposition of the C_2H_4 precursor, due to the short gas dwell time originating from the short flow distance and low pressure. This gas residence time is calculated to be much less than 1 s, preventing ethylene from undergoing any gas-phase rearrangement. Indeed, in situ mass spectroscopy at the sample position under the described growth conditions confirmed that the only carbon precursor touching the copper surface is C_2H_4, while Ar, H_2 and a trace amount of moisture are additionally present. (Figure 1b) This short stay can be critical to achieve uniformity over the entire wafer, as for longer stays C_2H_4 can get dissociated in the gas phase to other carbonaceous compounds, causing local variations on the precursor composition and altering the graphene growth mechanism.

Downloaded on 2016-02-09 to IP 131.111.5.15 address. Redistribution subject to ECS terms of use (see ecsdl.org/site/terms_use) unless CC License in place (see abstract).

The graphene films were transferred onto SiO_2 by selective etch of the copper substrate for Raman characterization (2, 19). Transferred films are characterized by micro Raman spectroscopy (Renishaw) using a 457-nm laser at 3 mW with a focal spot size of ca. 1.2 µm and also by 532-nm laser at 2 mW with a focal spot size of ca. 0.4 µm (Witec).

In order to characterize the surface morphology, we employed field emission scanning electron microscopy (SEM, Zeiss Gemini 1530 FEG) to image as-grown graphene films on copper foils. The mean graphene flake sizes were extracted and statistically processed from measurements of ca. 100 flakes on the SEM images. Similar statistical counting was also employed for angle and secondary nucleation size determination.

Results and Discussion

We tracked the graphene flake evolution over a time and temperature range that allows the flakes to be large enough to be observed by SEM and sparse enough to be analyzed as individual flakes. A time range of 0.5 min to 4 min and a temperature window of 770°C to 860°C with 30°C steps are well-fit for our purpose. In order to check any contamination or leakage, another growth under the similar condition but without any carbon source (C_2H_4) flow has also been performed to detect no graphene flakes, confirming that there is no leakage or contamination in the chamber. Figure 2 shows the SEM images of as-grown graphene flakes on copper foils.

The flake areas were measured and plotted versus time for each temperature (Figure 3a). The data is fitted by a modified Gompertz function (20). Qualitatively, a sigmoidal increase in flake size can be observed by increasing the time and temperature. The sigmoidal growth curves implicate the existence of two distinct and disparate growth regimes, before and after the inflection points. Shortly after C_2H_4 addition, nucleation takes place almost instantaneously. No new nucleation was observed after this instant. Following this primary nucleation, flakes begin to enlarge at an increasing pace until the inflection time point. This initial growth regime before the inflection point is in contrast with the expected growth originating from the ideal, defect-initiated crystallization from a supersaturated population of carbon adatoms. A similar behavior can be generally expected in the presence of deviations from the ideal crystallization, such as the effect of phospholipids lagging the crystallization of milk fat (17).

The double exponential in the Gompertz function is critical in understanding the mechanism behind this kinetic behavior. In Gompertz model, the rate of change of the area decays exponentially with time, which is analogous to the exponentially decaying rate constant of a reaction cascade with dispersive kinetics. Therefore, the fundamental mechanism that limits and governs the kinetic behavior should be a dispersive reaction system. As C_2H_4 in our case must go through a cascade of dissociation and dehydration reactions, we conclude that this cascade can be the rate governing mechanism.

Another critical factor in the Gompertz behavior is the proportionality of the growth rate with the flake size. This proportionality suggests that enlarging flakes actually supports the growth. We explain this by the effect of enhanced desorption of carbon containing species from the copper surface by sublimation. As the flakes enlarge they also prevent sublimation. This prevention is directly proportional with the flake area,

Downloaded on 2016-02-09 to IP 131.111.5.15 address. Redistribution subject to ECS terms of use (see ecsdl.org/site/terms_use) unless CC License in place (see abstract).

adding the area term in the Gompertz equation. Thus we believe that copper sublimation is a hindering factor for the graphene growth and it should be avoided.

Further analysis of the individual Gompertz fittings of the time-dependent growth data also provides information pertaining to the activation energy pathways. To extract the activation energy information from the Gompertz fits of Figure 3a, we first calculated the growth rates at each time point. However, using equivalent time scales without normalization for each growth temperature would be deceiving as the activation energy is a measure of particular growth reactions taking place at different times for each temperature. Therefore, the time variables of each curve have been rescaled with respect to the characteristic time scale at the inflection point, thereby aligning the growth rates that correspond to similar reactions (Figure 3b). This plot also confirms the initial increase in the growth rate attributed to the gradual change of the flake edge type from random to zigzag and also the post-inflection reduction of growth rates due to the depletion of the copper adsorbed carbon reactants.

The activation energy (E_A) is calculated by making an Arrhenius plot of the growth rate at the *inflection* points at each temperature (Figure 3, inset): 3.1 eV. To define the rate limiting step corresponding to this energy barrier, we account for the successive processes of; (i) hydrocarbon adsorption on copper, (ii) graphene lattice incorporation, (iii) surface diffusion, and (iv) catalytic C_2H_4 dissociation and dehydrogenation. It is highly unlikely that the process is limited by atomic carbon adsorption onto the dominant surface orientations on annealed copper foils as we did not detect significant pyrolysis of C_2H_4. Moreover, the associated energy barrier of C_2H_4 pyrolysis is extremely large (4.8 – 6.1 eV for Cu(111) and Cu(100)) (18). The energy barrier for hydrocarbon attachment on copper is an order of magnitude lower, (21) and as such it is far from our observed activation energies. Second, although the reports for the energy barrier for carbon adatom attachment to graphene are absent, the associated carbon attachment energy for ruthenium has been reported to be about 2 eV (22). making the attachment step unlikely to explain our determined activation energy. Diffusion effects can also be ruled out because the diffusion energy barriers for carbon adatom and dimer on copper are less than 0.1 eV and 0.5 eV, respectively (23). Lastly, as evidenced from the kinetic behavior, catalytic dissociative dehydrogenation of C_2H_4 on copper is the mechanism with higher activation energies, possibly explaining the observed value of 3.1 eV (24-27).

The results of the early-growth study aids in understanding the mechanisms but in order to obtain graphene useful for applications, a uniform continuous layer must be grown. One critical factor for the uniformity is the substrate crystallinity. We checked the surface crystalline orientation of the copper foils after the growth by electron back-scattering diffraction (EBSD). The copper surface consists of extremely large (mm-size) grains, which are (100) orientated and are close to parallel to the surface plane after the growthand the copper grain orientation is independent of the growth temperature and time (Figure 4a). Grain orientation maps display few grain boundaries but some lattice bending *ca.* 10º or more throughout the grains.

Figure 4b shows an example of continuous graphene monolayer, with some secondary layers seeded in hexagonal shapes. This observation indicates that when copper sublimation is absent the flake morphology is hexagonal, whereas the main graphene

Downloaded on 2016-02-09 to IP 131.111.5.15 address. Redistribution subject to ECS terms of use (see ecsdl.org/site/terms_use) unless CC License in place (see abstract).

layer has flakes having more random shapes due to the copper sublimation causing different growth rates at different directions with respect to the copper lattice.

Having studied the growth kinetics of graphene CVD, we scaled up the growth to 4-inch, 6-inch and 12-inch wafer scales. Uniformly covered graphene was obtained in all the three scales, corroborated by Raman mapping. Here, in Figure 5, we show the two-dimensional micro-Raman scans taken at different points on a 6-inch wafer (data at the other scales are not shown for proprietary reasons). While the maps show similar texture, the quantitative analysis of G'/G peak intensity ratios indicate that our graphene is uniformly monolayer. Importantly, our scaled-up graphene is high in quality with an average D/G peak intensity ratio < 0.09.

Conclusions

The fundamental mechanism that governs the kinetics of the CVD growth of graphene is the catalytic dissociative dehydration of ethylene on copper surface. This finding along with the sigmoidal growth curves indicate that the flake growth is driven by a continual feed of hydrocarbons to the surface, not by an initial carbon supersaturation. Copper sublimation is found to hinder the growth by enhancing desorption of carbonaceous species from the surface. Under optimized production conditions in a vertical fast-flow CVD furnace, 6-inch wafer-scale graphene uniformity is also demonstrated.

Downloaded on 2016-02-09 to IP 131.111.5.15 address. Redistribution subject to ECS terms of use (see ecsdl.org/site/terms_use) unless CC License in place (see abstract).

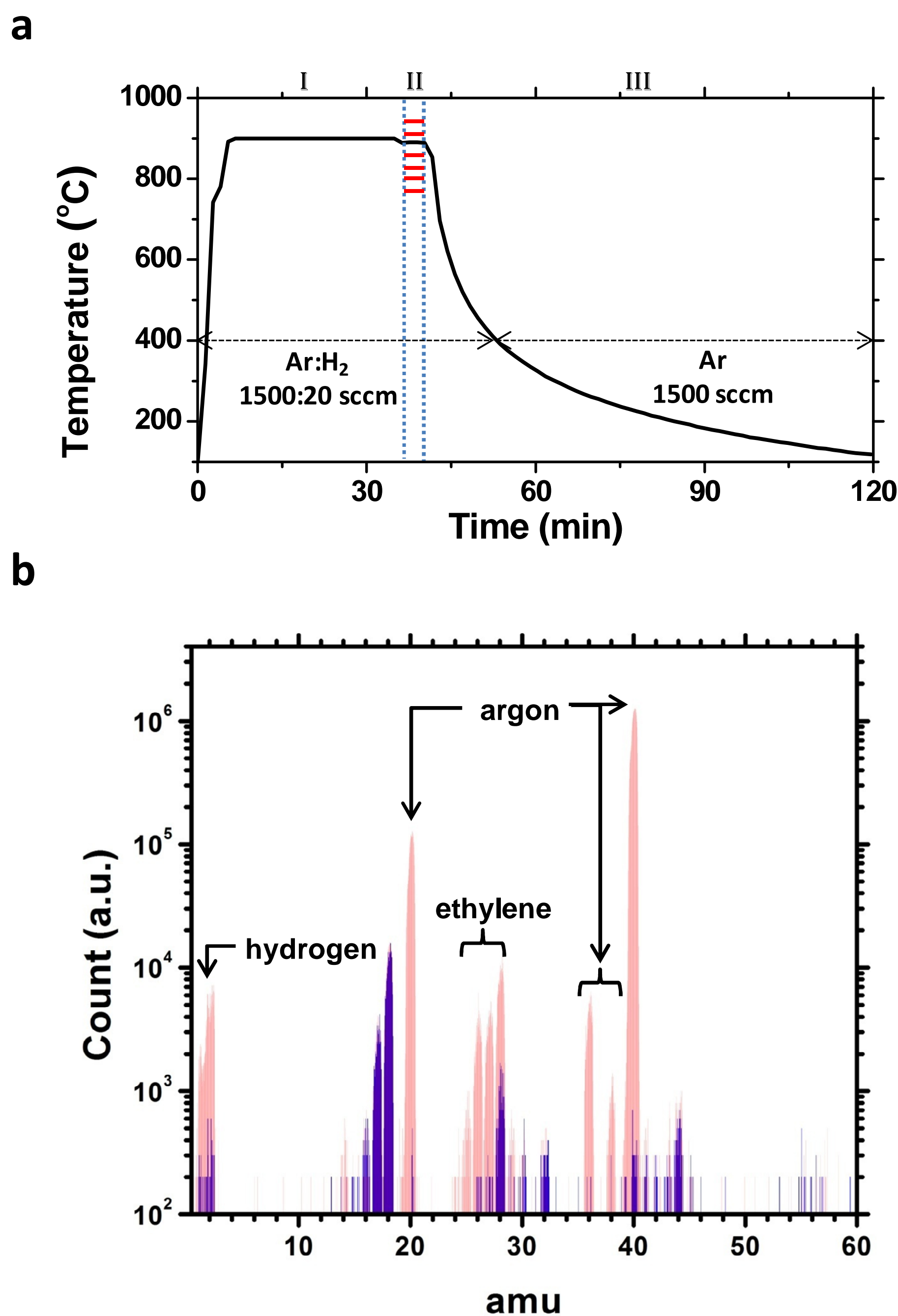

Figure 1. (a) A typical CVD growth scheme, black curve shows the actual temperature measured by the infrared detector. (b) Mass spectroscopy of the gas species at the sample position under growth conditions.

Downloaded on 2016-02-09 to IP 131.111.5.15 address. Redistribution subject to ECS terms of use (see ecsdl.org/site/terms_use) unless CC License in place (see abstract).

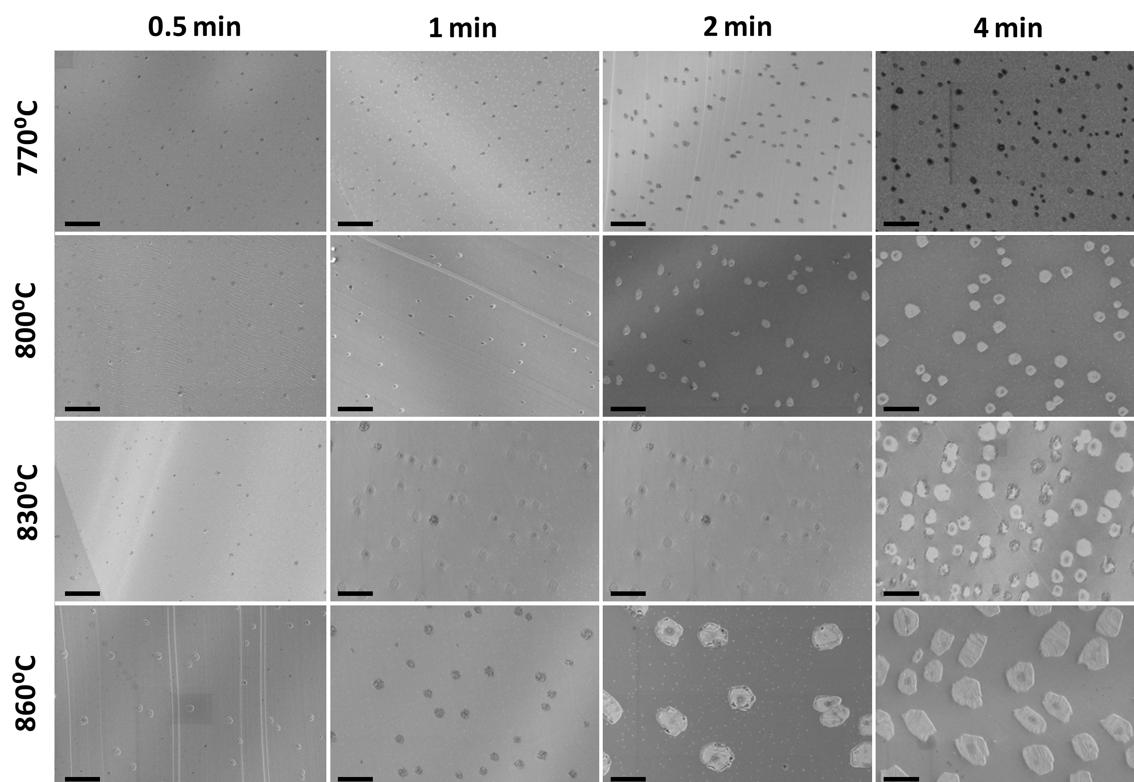

Figure 2. SEM images of the as-grown graphene flakes on Cu foils for varied growth time and temperatures. Scalebar is 2µm.

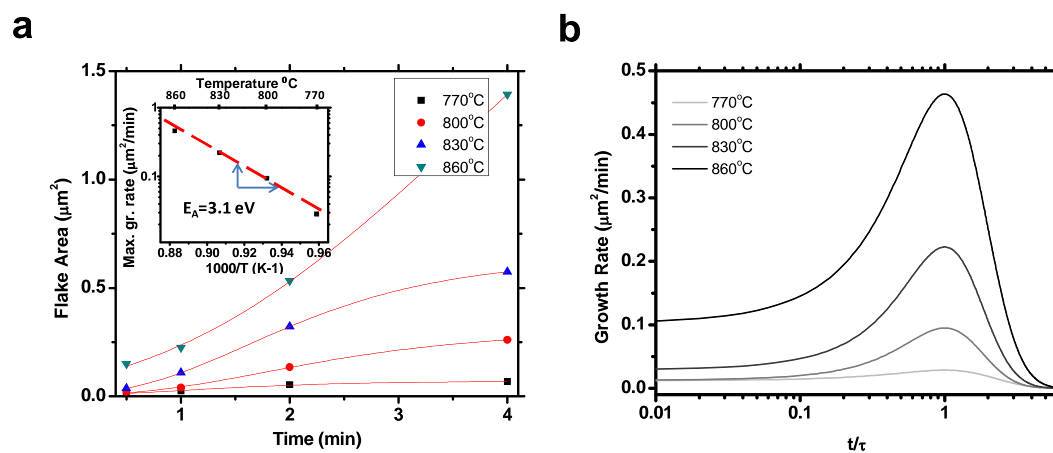

Figure 3. (a) Graphene flake area *vs.* growth time. Lines are the Gompertz fittings to the SEM data. Inset: Arrhenius plot of the growth rate at the inflection points of the Gompertz fittings. (b) Growth rates *vs.* normalized time (τ is the normalization factor, the time at the inflection point of the area fit for each temperature)

Downloaded on 2016-02-09 to IP 131.111.5.15 address. Redistribution subject to ECS terms of use (see ecsdl.org/site/terms_use) unless CC License in place (see abstract).

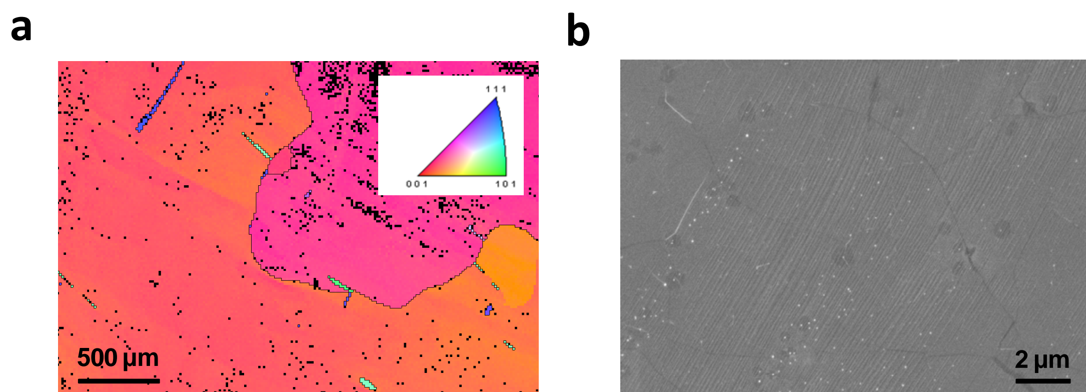

Figure 4. (a) EBSD map of the copper foil after growth (with 30 min anneal at 900°C). Inset: The color map for crystalline orientations. (b) SEM image of the continuous graphene with several small hexagonal secondary layers.

Downloaded on 2016-02-09 to IP 131.111.5.15 address. Redistribution subject to ECS terms of use (see ecsdl.org/site/terms_use) unless CC License in place (see abstract).

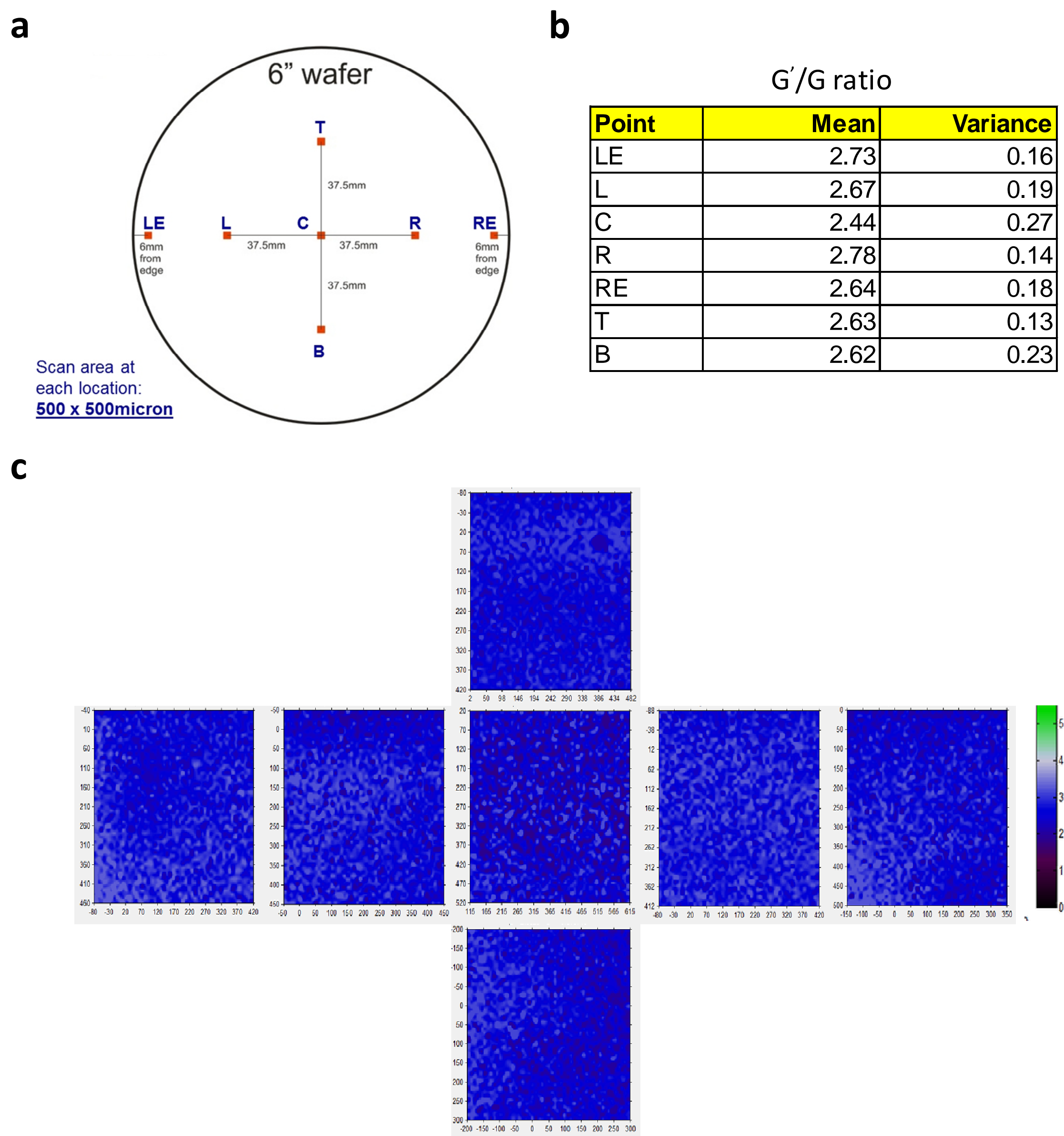

Point	Mean	Variance
LE	2.73	0.16
L	2.67	0.19
C	2.44	0.27
R	2.78	0.14
RE	2.64	0.18
T	2.63	0.13
B	2.62	0.23

Figure 5. (a) Schematic of the wafer to show the position of the scanned areas. (b) *G′/G* peak intensity ratios corresponding to the scanned areas. (c) Two-dimensional micro Raman maps of the *G′/G* peak intensity ratio for the scanned areas corresponding to the indicated positions in (a). Scan area at each location is 500 × 500 μm.

Acknowledgments

The authors appreciate the support from Binnig Rohrer Nanotechnology Center of ETH Zürich and IBM Zürich. K. Kunze at the electron microscopy center of ETH (EMEZ), H. Ma and R. Spolenak are thanked for their efforts to obtain EBSD data. M.T.C. thanks the Isaac Newton Trust, Trinity College Cambridge, for generous financial support. K.B.K.T., P.G. and J.R. acknowledge the funding from the EU project Grafol.

Downloaded on 2016-02-09 to IP 131.111.5.15 address. Redistribution subject to ECS terms of use (see ecsdl.org/site/terms_use) unless CC License in place (see abstract).

References

1. S. Bae, H. Kim, Y. Lee, X. Xu, J.-S. Park, Y. Zheng, J. Balakrishnan, T. Lei, H. Ri Kim, Y. I. Song, Y.-J. Kim, K. S. Kim, B. Ozyilmaz, J.-H. Ahn, B. H. Hong and S. Iijima, *Nat Nano*, **5**, 574 (2010).
2. X. Li, W. Cai, J. An, S. Kim, J. Nah, D. Yang, R. Piner, A. Velamakanni, I. Jung, E. Tutuc, S. K. Banerjee, L. Colombo and R. S. Ruoff, *Science*, **324**, 1312 (2009).
3. X. Li, C. W. Magnuson, A. Venugopal, J. An, J. W. Suk, B. Han, M. Borysiak, W. Cai, A. Velamakanni, Y. Zhu, L. Fu, E. M. Vogel, E. Voelkl, L. Colombo and R. S. Ruoff, *Nano Lett.*, **10**, 4328 (2010).
4. G.-X. Ni, Y. Zheng, S. Bae, H. R. Kim, A. Pachoud, Y. S. Kim, C.-L. Tan, D. Im, J.-H. Ahn, B. H. Hong and B. Özyilmaz, *ACS Nano*, **6**, 1158 (2012).
5. A. W. Tsen, L. Brown, M. P. Levendorf, F. Ghahari, P. Y. Huang, R. W. Havener, C. S. Ruiz-Vargas, D. A. Muller, P. Kim and J. Park, *Science*, **336**, 1143 (2012).
6. C. Mattevi, H. Kim and M. Chhowalla, *J. Mater. Chem.*, **21**, 3324 (2011).
7. X. Li, W. Cai, L. Colombo and R. Ruoff, *Nano Lett.*, **9**, 4268 (2009).
8. J. M. Wofford, S. Nie, K. F. McCarty, N. C. Bartelt and O. D. Dubon, *Nano Lett.*, **10**, 4890 (2010).
9. L. Liu, H. Zhou, R. Cheng, Y. Chen, Y.-C. Lin, Y. Qu, J. Bai, I. A. Ivanov, G. Liu, Y. Huang and X. Duan, *J. Mater. Chem.*, **22**, 1498 (2012).
10. H. Kim, C. Mattevi, M. R. Calvo, J. C. Oberg, L. Artiglia, S. Agnoli, C. F. Hirjibehedin, M. Chhowalla and E. Saiz, *ACS Nano*, **6**, 3614 (2012).
11. M. Avrami, *J. Chem. Phys.*, **7**, 1103 (1939).
12. M. Lin, J. P. Ying Tan, C. Boothroyd, K. P. Loh, E. S. Tok and Y.-L. Foo, *Nano Lett.*, **6**, 449 (2006).
13. C. P. Winsor, *Proc. Natl. Acad. Sci. U. S. A.*, **18**, 1 (1932).
14. K. Chaleepa, A. Szepes and J. Ulrich, *Chem. Phys. Lipids*, **163**, 390 (2010).
15. I. Foubert, K. Dewettinck and P. A. Vanrolleghem, *Trends Food Sci. Technol.*, **14**, 79 (2003).
16. W. Kloek, P. Walstra and T. van Vliet, *J. Am. Oil Chem. Soc.*, **77**, 389 (2000).
17. B. Vanhoutte, K. Dewettinck, I. Foubert, B. Vanlerberghe and A. Huyghebaert, *Eur. J. Lipid Sci. Technol.*, **104**, 490 (2002).
18. L. Zhao, K. T. Rim, H. Zhou, R. He, T. F. Heinz, A. Pinczuk, G. W. Flynn and A. N. Pasupathy, *Solid State Commun.*, **151**, 509 (2011).
19. A. Reina, X. Jia, J. Ho, D. Nezich, H. Son, V. Bulovic, M. Dresselhaus and J. Kong, *Nano Lett.*, **9**, 30 (2009).
20. M. Zwietering, I. Jongenburger, F. Rombouts and K. Van't Riet, *Appl. Environ. Microbiol.*, **56**, 1875 (1990).
21. W. Zhang, P. Wu, Z. Li and J. Yang, *arXiv:1101.3851* (2011).
22. E. Loginova, N. C. Bartelt, P. J. Feibelman and K. F. McCarty, *New J. Phys.*, **10**, 093026 (2008).
23. P. Wu, W. Zhang, Z. Li, J. Yang and J. G. Hou, *J. Chem. Phys.*, **133**, 071101 (2010).
24. J. H. Sinfelt, J. L. Carter and D. J. C. Yates, *J. Catal.*, **24**, 283 (1972).
25. J. L. Franklin and F. H. Field, *J. Chem. Phys.*, **21**, 2082 (1953).
26. J. H. Sinfelt and D. J. C. Yates, *J. Catal.*, **8**, 82 (1967).
27. Y. Chen and D. G. Vlachos, *J. Phys. Chem. C*, **114**, 4973 (2010).

Downloaded on 2016-02-09 to IP 131.111.5.15 address. Redistribution subject to ECS terms of use (see ecsdl.org/site/terms_use) unless CC License in place (see abstract).